



## PAPER

## QCD at finite chemical potential in and out-of equilibrium

## OPEN ACCESS

RECEIVED  
28 March 2021

REVISED  
10 November 2021

ACCEPTED FOR PUBLICATION  
22 November 2021

PUBLISHED  
30 November 2021

Original content from this work may be used under the terms of the [Creative Commons Attribution 4.0 licence](#).

Any further distribution of this work must maintain attribution to the author(s) and the title of the work, journal citation and DOI.



Olga Soloveva<sup>1</sup> , Pierre Moreau<sup>2</sup> and Elena Bratkovskaya<sup>1,3,4</sup>

<sup>1</sup> Institute for Theoretical Physics, University of Frankfurt, Frankfurt, Germany

<sup>2</sup> Department of Physics, Duke University, Durham, NC 27708, United States of America

<sup>3</sup> GSI, Helmholtzzentrum für Schwerionenforschung GmbH, Darmstadt, Germany

<sup>4</sup> Helmholtz Research Academy Hesse for FAIR (HFHF), GSI Helmholtz Center for Heavy Ion Physics, Campus Frankfurt, 60438 Frankfurt, Germany

E-mail: [E.Bratkovskaya@gsi.de](mailto:E.Bratkovskaya@gsi.de)

**Keywords:** quark-gluon plasma, heavy-ions, transport models

## Abstract

We review the transport properties of the strongly interacting quark-gluon plasma (QGP) created in heavy-ion collisions at ultrarelativistic energies, i.e. out-of-equilibrium, and compare them to the equilibrium properties. The description of the strongly interacting (non-perturbative) QGP in equilibrium is based on the effective propagators and couplings from the Dynamical QuasiParticle Model (DQPM) that is matched to reproduce the equation-of-state of the partonic system above the deconfinement temperature  $T_c$  from lattice QCD. We study the transport coefficients such as the ratio of shear viscosity and bulk viscosity over entropy density, diffusion coefficients, electric conductivity etc versus temperature  $T$  and baryon chemical potential  $\mu_B$ . Based on a microscopic transport description of heavy-ion collisions we, furthermore, discuss which observables are sensitive to the QGP formation and its properties.

## 1. Introduction

Numerous achievements of heavy-ion collision (HIC) experiments have dramatically changed the theoretical understanding of the QCD matter properties, especially the deconfined QCD matter created in the central interaction volume at relativistic energies. Initially the deconfined QCD matter—or the Quark-Gluon-Plasma (QGP)—has been considered as a weakly interacting system of massless partons (quarks and gluons) which might be described by perturbative QCD (pQCD). Measurements of the anisotropic particle flow and jet quenching at the Relativistic Heavy-Ion Collider (RHIC) revealed that in the vicinity of the quark-hadron phase transition the deconfined state of QCD matter (at high temperature and partonic density) behaves as a nearly perfect relativistic fluid with the lowest value of the specific shear viscosity among the known fluids [1–4]. Actual and future heavy-ion collision experiments will probe the QCD phase diagram at nonzero baryon density (or baryon chemical potential  $\mu_B$ ). At ultra-relativistic energies at the Large Hadron Collider (LHC) or the Relativistic Heavy-Ion Collider (RHIC) the quark-gluon plasma is formed with nearly zero baryon chemical potential and the phase transition from the partons to the hadrons is a rapid crossover. In order to quantify experimental findings one can employ transport or hydrodynamic simulations that successfully describe the differential distributions of produced particles in these HICs.

While there are a plethora of studies about the QCD medium in the confined hadronic phase the future facilities will explore the QCD medium at high net baryon density or baryon chemical potential. The QCD phase diagram can be understood from the thermodynamic point of view in terms of the temperature  $T$  and baryon chemical potential  $\mu_B$ , where the most unexplored region is located at moderate temperatures and relatively high  $\mu_B$ . This region is of particular interest in the Beam Energy Scan programs at RHIC [5] as well as the future experimental program of FAIR (Facility for Antiproton and Ion Research) [6] at GSI and the NICA (Nuclotron-based Ion Collider fAcility) facility at JINR [7]. In the region of vanishing baryon chemical potential one can apply lattice QCD (lQCD) techniques to describe the macroscopic properties of the QCD medium such as the equation of state; moreover one can extract transport coefficients of the QCD medium at  $\mu_B = 0$ . A primary

difficulty in dealing with non-zero baryon chemical potentials is the fermion sign problem for QCD (the fermion determinant is not positive definite), which makes the current lattice QCD methods inapplicable in the low  $T$  and finite  $\mu_B$  region.

An alternative approach, which can describe microscopic properties of the deconfined QCD medium in a wide range of baryon chemical potentials, is to use effective models on the basis of ‘resummed’ propagators and couplings. In this work we review the results of the transport properties and the evolution of the QCD medium at finite chemical potential  $\mu_B$  in equilibrium while for the description of the deconfined phase—near and out equilibrium—effective models and the PHSD transport approach are applied. Considering the transport coefficients and the EoS of the QGP phase we compare our results with the various results from the literature at vanishing chemical potential.

To quantify the strongly-interacting liquid one can apply hydrodynamic descriptions of the system. However, in order to perform hydrodynamical simulations of the time evolution of the quark-gluon matter at finite baryon chemical potential, one needs to estimate or know the transport coefficients of the matter in this region. The evaluation of the transport coefficients at finite  $\mu_B$  depends on the underlying microscopic theory which describes the interaction between quarks and gluons, but we face a fundamental problem to construct and evaluate such a theory at finite  $T$  and  $\mu_B$  from first principles.

## 2. Microscopic properties of the QGP at finite chemical potential

For the full description of the QGP dynamics one needs to estimate first the microscopic properties of the relevant degrees of freedom such as the effective masses (and widths) of the partonic propagators as well as elastic cross-sections for the different partons. In the region of finite  $T$  and moderate baryon chemical potential  $\mu_B$  one can rely on the estimates from effective models. Here we consider the essential features of the QGP medium in terms of strongly interacting quarks and gluons as given by the dynamical quasi-particle model (DQPM) [8–10]. The DQPM reproduces the equation of state of the partonic system above the deconfinement temperature  $T_c$  from lattice Quantum Chromodynamics (QCD) and predicts reasonable estimates for the QGP transport coefficients, which—as we will see later—are in agreement with the IQCD results available at  $\mu_B = 0$ .

In the DQPM the quasi-particles are characterized by dressed propagators with complex self-energies, where the real part of the self-energies is related to dynamically generated thermal masses, while the imaginary part provides information about the lifetime and reaction rates of the partons (interaction widths),

$$G_j^R(\omega, \mathbf{p}) = \frac{1}{\omega^2 - \mathbf{p}^2 - M_j^2 + 2i\gamma_j\omega}, \quad (1)$$

using  $\omega = p_0$  for energy, while  $M_j$  and  $\gamma_j$  are the thermal mass and width of a parton. In the DQPM the spectral functions of the quasiparticles  $\rho_j$  ( $j = q, \bar{q}, g$ ) or imaginary parts of the propagator  $\rho_j = -2 \text{Im}(G_j^R)$  are no longer  $\delta$ -functions in the invariant mass squared but given by

$$\rho_j(\omega, \mathbf{p}) = \frac{4\omega\gamma_j}{(\omega^2 - \mathbf{p}^2 - M_j^2)^2 + 4\gamma_j^2\omega^2} \quad (2)$$

separately for quarks, antiquarks and gluons ( $j = q, \bar{q}, g$ ).

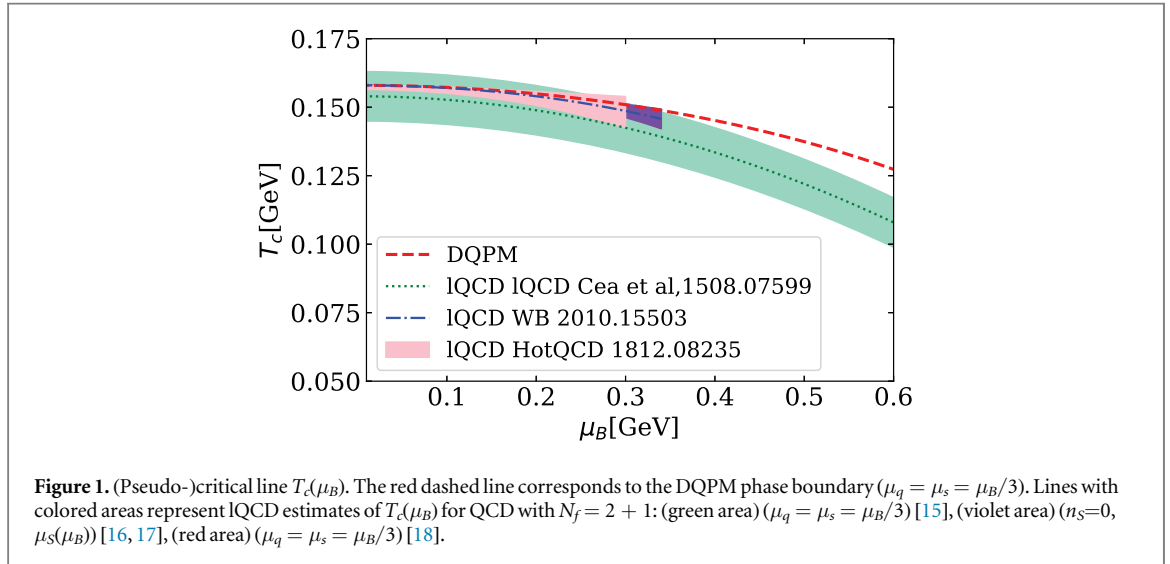
All the microscopic properties as well as transport coefficients of the QCD matter are sensitive to the underlying coupling of the matter, which can be estimated within the DQPM using the entropy density from IQCD at  $\mu_B = 0$ . Although the coupling constant  $g^2$  in general depends on temperature and baryon chemical potential, we start with the determination of  $g^2(T, \mu_B = 0)$ . The temperature dependence is parameterized via the entropy density  $s(T, \mu_B = 0)$  from lattice QCD from [11, 12] in the following way:

$$g^2(T, \mu_B = 0) = d((s(T, 0)/s_{\text{SB}}^{\text{QCD}})^e - 1)^f, \quad (3)$$

with the Stefan-Boltzmann entropy density  $s_{\text{SB}}^{\text{QCD}} = 19/9 \pi^2 T^3$  and the dimensionless parameters  $d = 169.934$ ,  $e = -0.178434$  and  $f = 1.14631$ . In order to obtain the coupling at finite baryon chemical potential  $\mu_B$ , we use the ‘scaling hypothesis’ introduced in [13], which assumes that  $g^2$  is a function of the ratio of the effective temperature  $T^* = \sqrt{(T^2 + \mu_q^2/\pi^2)^{1/2}}$  (where quark chemical potential is defined as follows  $\mu_q = \mu_u = \mu_s = \mu_B/3$ ) and the  $\mu_B$ -dependent critical temperature  $T_c(\mu_B)$  as [14]

$$g^2(T/T_c, \mu_B) = g^2\left(\frac{T^*}{T_c(\mu_B)}, \mu_B = 0\right), \quad (4)$$

with  $T_c(\mu_B) = T_c(1 - \alpha\mu_B^2)^{1/2}$  being the (pseudo)critical line of the DQPM (shown as red dashed line figure 1), where  $T_c$  is the critical temperature at vanishing chemical potential ( $\approx 0.158$  GeV) and  $\alpha = 0.974 \text{ GeV}^{-2}$ .



In figure 1 we compare the (pseudo-)critical lines of the DQPM with the IQCD calculations (for QCD with  $N_f = 2 + 1$ ) which are shown as lines with colored areas: (violet area) ( $n_s=0$ ,  $\mu_s(\mu_B)$ ) [16, 17] and (red area) [18] ( $\mu_q = \mu_s = \mu_B/3$ ). One can see that the DQPM line is in the range of the IQCD errorbars. For completeness we also show the IQCD estimates from [15] ( $\mu_q = \mu_s = \mu_B/3$ )—green area, however, note that these IQCD results have been obtained by the method of analytic continuation from imaginary to real chemical potentials for large  $\mu_B$ , which can lead to large systematic errors.

One can define the real part of the partonic self-energies by the dynamical quasi-particle masses (for gluons and quarks) which are given by the HTL thermal masses in the asymptotic high-momentum regime by [19, 20]

$$m_g^2(T, \mu_B) = \frac{g^2(T, \mu_B)}{6} \left( \left( N_c + \frac{N_f}{2} \right) T^2 + \frac{N_c}{2} \sum_q \frac{\mu_q^2}{\pi^2} \right) \quad (5)$$

$$m_{q(\bar{q})}^2(T, \mu_B) = \frac{N_c^2 - 1}{8N_c} g^2(T, \mu_B) \left( T^2 + \frac{\mu_q^2}{\pi^2} \right), \quad (6)$$

where  $N_c = 3$  and  $N_f = 3$  denote the number of colors and the number of flavors respectively. The strange quark has a larger bare mass which needs to be considered in its dynamical mass. Empirically we find  $m_s(T, \mu_B) = m_{u/d}(T, \mu_B) + \Delta m$  and  $\Delta m \approx 30$  MeV. Furthermore, the quasi-particles in the DQPM have thermal widths, which are adopted in the form [14, 20]

$$\gamma_j(T, \mu_B) = \frac{1}{3} C_j \frac{g^2(T, \mu_B) T}{8\pi} \ln \left( \frac{2c_m}{g^2(T, \mu_B)} + 1 \right), \quad (7)$$

where we use the QCD color factors for quarks,  $C_q = \frac{N_c^2 - 1}{2N_c} = 4/3$ , and for gluons  $C_g = N_c = 3$ . Further, we fixed the parameter  $c_m = 14.4$ , which is related to a magnetic cut-off. We assume that all (anti-)quarks have the same thermal width  $\gamma_u = \gamma_d = \gamma_s$ . Fixing the quasi-particle properties as described above, one can estimate the quasi-particles entropy density  $s^{\text{dqp}}$  and quark number density  $n^{\text{dqp}}$  in the 2loop  $\Phi$ derivable approximation from Baym [21, 22], whereas  $s = s^{\text{dqp}}$  and  $n_B = n^{\text{dqp}}/3$ . Then we can obtain other thermodynamic quantities such as the entropy density  $s(T, \mu_B)$ , the pressure  $P(T, \mu_B)$  and energy density  $\epsilon(T, \mu_B)$ . We obtain the pressure  $P$  at finite  $T$  and  $\mu_B$  by using the Maxwell relation of a grand canonical ensemble:

$$P(T, \mu_B) = P(T_0, 0) + \int_{T_0}^T s(T', 0) dT' + \int_0^{\mu_B} n_B(T, \mu_B') d\mu_B', \quad (8)$$

where the lower bound in temperature is chosen between  $0.1 < T_0 < 0.15$  GeV. The energy density  $\epsilon$  then follows from the Euler relation

$$\epsilon = Ts - P + \mu_B n_B. \quad (9)$$

The differential cross section for a binary process of on-shell particles ( $i + j \rightarrow c + d$ ) in the center-of-momentum frame (CM), where the momenta of the colliding particles obey  $\mathbf{k}_i + \mathbf{k}_j = \mathbf{p}_c + \mathbf{p}_d = \mathbf{P} = 0$  and  $k_i^0 + k_j^0 = \sqrt{s} = p_c^0 + p_d^0$ , reads

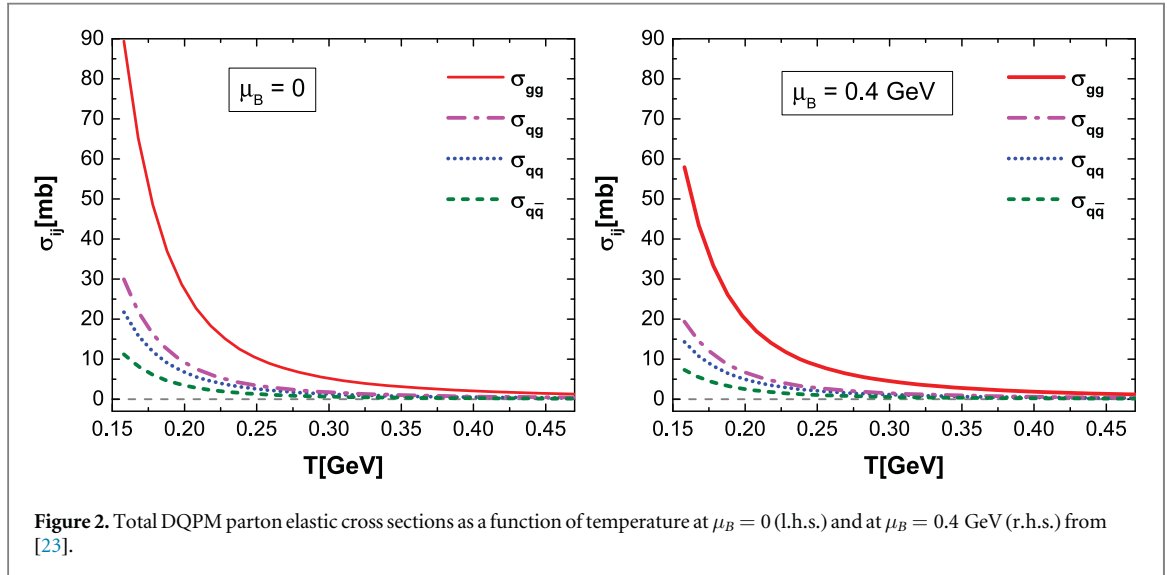


**Figure 2.** Total DQPM parton elastic cross sections as a function of temperature at  $\mu_B = 0$  (l.h.s.) and at  $\mu_B = 0.4$  GeV (r.h.s.) from [23].

$$d\sigma_{ij \rightarrow cd}^{on}(\sqrt{s}, \Omega) = \frac{1}{64\pi^2 s} \frac{p_{out}}{p_{in}} |\bar{\mathcal{M}}|^2 d\Omega, \quad (10)$$

where  $|\bar{\mathcal{M}}|^2 \equiv |\bar{\mathcal{M}}(k_{i_1} \dots k_{i_n} \rightarrow p_{j_1} \dots p_{j_m})|^2$  denotes the invariant matrix element squared averaged over the color and spin of the incoming particles and summed over those of the final particles. In (10)  $d\Omega$  is the differential solid angle corresponding to one of the final particles. The momenta of the initial/final ( $p_{in/out}$ ) particles in the CM frame are given by

$$p_i = \frac{\sqrt{(s - (m_i + m'_i)^2)(s - (m_i - m'_i)^2)}}{2\sqrt{s}}, \quad (11)$$

where  $i = in/out$ ,  $m_i$  and  $m'_i$  being the masses of the colliding partons.

The total cross section is obtained via:

$$\sigma_{tot}^{ij \rightarrow cd}(\sqrt{s}) = \frac{1}{32\pi s} \frac{p_{out}}{p_{in}} \gamma_{ij} \int_{-1}^1 d \cos(\theta) |\bar{\mathcal{M}}|^2, \quad (12)$$

where  $\theta$  is the final polar angle of one of the final particles in the CM frame, and  $\gamma_{ij} = 1 - \frac{1}{2}\delta_{ij}$  is the symmetry factor.

The DQPM total cross-sections for different channels are shown in figure 2 as a function of temperature for  $\mu_B = 0$  and  $\mu_B = 0.4$  GeV. The total cross sections at fixed  $\sqrt{s}$  depend on temperature as  $\sigma_{tot}^{ij \rightarrow cd} \sim 1/T^3$  or  $\sim 1/T^4$ , which is governed by the  $T$ -dependence of the DQPM running coupling. The difference in the  $T$ -dependence for different channels arises from the combinations of  $s$ -,  $t$ -,  $u$ - channels: for  $q-q$ ,  $q-\bar{q}$  and  $q-g$  scatterings  $\sigma_{tot}^{ij \rightarrow cd} \sim 1/T^3$ , while for the  $g-g$  channel the terms  $1/T^3$ ,  $1/T^4$  have equivalent contributions to the total cross-section  $\sigma_{tot}^{ij \rightarrow cd} \sim c_3/T^3 + c_4/T^4$ , where  $c_3, c_4$  depend on  $\sqrt{s}$ ,  $\mu_B$ . The cross-sections decrease with the increase of baryon chemical potential as expected from the  $\mu_B$  dependence of the DQPM coupling. This trend is in agreement with the pQCD predictions for high temperatures and chemical potential, where the QGP can be described approximately by a free gas of quarks and gluons. We have found that the collisional widths from the DQPM and those evaluated from the interaction rates—by calculating the partonic differential cross-sections as a function of  $T$  and  $\mu_B$  for the leading tree-level diagrams—are in reasonable agreement. Accordingly, the quasi-particle limit holds sufficiently well [23].

For the scatterings of the on-shell partons (i.e. the energies of the particles are taken to be  $E^2 = \mathbf{p}^2 + M^2$  with  $M$  being the pole mass) the interaction rate  $\Gamma^{on}$  is obtained as follows,

$$\Gamma_i^{on}(p_i, T, \mu_q) = \sum_{j=q,\bar{q},g} \int \frac{d^3 p_j}{(2\pi)^3} d_j f_j v_{rel} \int d\sigma_{ij \rightarrow cd}^{on} (1 \pm f_c)(1 \pm f_d), \quad (13)$$

where  $v_{rel} = \frac{\sqrt{(p_i - p_j)^2 - m_i^2 m_j^2}}{E_i E_j}$  denotes the relative velocity in the c.m. frame,  $d_j$  is the degeneracy factor for spin and color (for quarks  $d_q = 2 \times N_c$  and for gluons  $d_g = 2 \times (N_c^2 - 1)$ ), using the shorthand notation  $f_j = f_j(E_j, T, \mu_q)$  for the distribution functions. In equation (13) and in all the following sections, the notation  $\sum_{j=q,\bar{q},g}$  includes the contribution from all possible partons which in our case are the gluons and the (anti-)quarks of three different flavors ( $u, d, s$ ). The parton interaction rate  $\Gamma_i^{on}(p_i, T, \mu_q)$  can be used for the estimation of the parton relaxation time, which is the key ingredient for transport coefficients from kinetic theory.

### 3. Transport coefficients of the QCD at finite chemical potential

We first focus on the the transport coefficients at vanishing baryon chemical potential and present the dimensionless ratio of the shear and bulk viscosities to the entropy density, i.e.,  $\eta/s$  and  $\zeta/s$ , the scaled electric conductivity  $\sigma_Q/T$ , as well as the scaled baryon-diffusion coefficient  $\kappa_B/T^2 = \sigma_B/T$ . The results for the ratios  $\eta/s$  and  $\zeta/s$  as well as  $\sigma_Q/T$  are in accord with the available results from the IQCD calculations at  $\mu_B = 0$ .

The most popular transport coefficients—shear and bulk viscosities—have been evaluated within various models in the hadronic and the partonic phase. The shear viscosity reflects the strength of the interaction inside the QGP medium; it can be related to the parton interaction rates, which is a challenge to evaluate on the basis of first principles. Various theoretical models show that the temperature dependence of the QCD specific shear viscosity is qualitatively different in the confined and deconfined phases. Starting from the hadronic phase below the pseudo-critical temperature  $T < T_c$ ,  $\eta/s$  monotonically decreases with  $T$  because the system is dominated by pions with weaker interactions at lower  $T$ . For the partonic phase above the pseudo-critical temperature  $T > T_c$ ,  $\eta/s$  increases with temperature because the interaction attenuates at high  $T$ . Approaching the phase transition from hadronic to partonic phase at vanishing chemical potential the specific shear viscosity shows a dip followed by an increase with temperature. A similar temperature dependence of the specific shear viscosity  $\eta/s$  is also seen for other fluids such as  $H_2O$  and  $He$ .

While first only the shear viscosity was considered in the hydrodynamical simulations it was found later that the bulk viscosity of the QGP should be non-zero, at least in the vicinity of the phase transition [24]. The bulk viscosity reduces the speed of the radial expansion and thus influences the mean momentum of produced particles. It is known that the bulk viscosity is identically zero in conformal fluids and it is expected that the QCD medium converges a conformal behaviour in the high-energy or temperature regime. Nevertheless, the IQCD results on the enhanced trace anomaly close to  $T_c$  have shown that it is probably not the case for the deconfined QCD medium in the vicinity of the phase transition.

The transport coefficients of the QCD matter can be obtained within the Kubo formalism [25, 26], which was used to calculate the viscosities for a previous version of the DQPM within the PHSD transport approach in a box with periodic boundary conditions (cf [27]). The method becomes notoriously difficult for the partonic phase. A more simple way to estimate the transport coefficient is to imply the effective Boltzmann equation in the relaxation-time approximation (RTA) [28] from the collisional widths. As has been shown in [23, 27] the both methods agree rather well for the ratios  $\eta/s$  and  $\zeta/s$ .

In figure 3 we show the DQPM results (red lines) for the ratios of specific shear  $\eta$  (left) and bulk  $\zeta$  (right) viscosities over entropy density  $s$  for the QGP phase as a function of the scaled temperature  $T/T_c$  at  $\mu_B = 0$  evaluated within the RTA. We find that the DQPM ratios of  $\eta/s$  and  $\zeta/s$  are in a good agreement with the IQCD data for pure SU(3) gauge theory (dark blue pentagons) [29, 30], (light green triangles and dark red squares) [31], (orange circles) [32], (violet triangles) [31], (dark cyan squares) [33]. For comparison we display also the estimates from non-conformal holographic models [34, 35] and the far-from-equilibrium time-dependent value of  $\eta/s$  in a holographic model (in the region of average time  $t_{avg} = 0.24 - 0.59$  fm) [36] as well as the results from the Bayesian analysis of the experimental data from heavy-ion collisions [37].

Moreover, we show the results for the hadronic phase from the transport models URQMD (orange line with open circles) [42] and SMASH (grey solid line with rhombuses) [43, 44]. The PHSD results for the hadronic phase are shown by the violet solid line with triangles and for the partonic phase by violet solid line with circles [27]. The specific shear viscosity for the partonic phase from the PHSD is in a good agreement with the estimates from the DQPM, while in case of the bulk viscosity the previous PHSD result is higher than the actual DQPM calculations. This is related to the fact that in the early PHSD study in [27] the QGP phase has been realized with a DQPM parametrization with slightly different quasiparticle properties (masses and widths) that have been fitted to the entropy density of earlier IQCD data [45]. Also the present DQPM partonic cross sections are evaluated from leading order scattering diagrams and depend on  $T$ ,  $\mu_B$ ,  $\sqrt{s}$  and the scattering angle while the previous cross sections in [27] were only depending on the energy density, i.e. on temperature. The differences show up more pronounced in the bulk viscosity than in the shear viscosity due to the terms related to the mass derivative and speed of sound  $c_s^2$  in the expression for the bulk viscosity which are sensitive to the actual form of the temperature dependence of the masses and cross sections.

The ratio  $\eta/s$  in the hadronic phase decreases when approaching the phase transition temperature  $T_c$ . One can see a difference in the vicinity of the phase transition in the  $T$ -dependence for the transport models, which can be attributed to differences in the evaluation of the viscosities as well as difference between the transport model descriptions. Additionally, we show the RTA calculations from the  $N_f = 2$  linear sigma model (for a vacuum sigma mass  $m_0 = 600$  MeV) [40] and the  $N_f = 3$  PNJL model [41].

Furthermore, the electric conductivity and baryon conductivity of QGP matter, produced in HICs, are of fundamental importance. It is known that the electric conductivity determines the soft photon spectra [20, 46, 47] and is directly related to their emission rate [48]. Moreover, the electric conductivity affects the



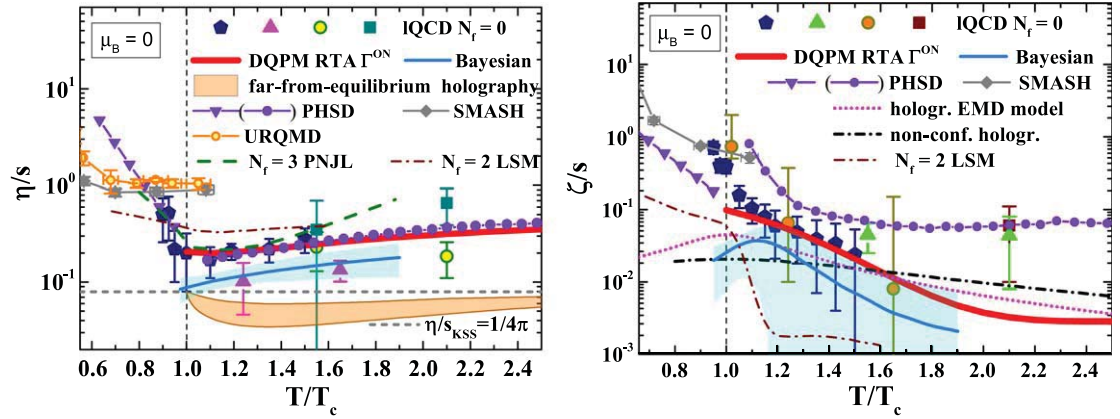


**Figure 3.** Specific shear (left) and bulk (right) viscosities as a function of the scaled temperature  $T/T_c$  at  $\mu_B = 0$ . The DQPM results—obtained by the RTA approach with the interaction rate [38]—are presented by the red solid lines while the dashed gray line demonstrates the KovtunSonStarinets bound  $(\eta/s)_{KSS} = 1/(4\pi)$  [39]. The symbols corresponds to the IQCD results for pure SU(3) gauge theory (dark blue pentagons) [29, 30], (light green triangles and dark red squares) [31], (orange circles) [32], (violet triangles) [31], (dark cyan squares) [33]. The solid blue lines show the results from a Bayesian analysis of experimental heavy-ion data [37]. The light magenta dotted line corresponds to the estimates from the Einstein-Maxwell-Dilaton (EMD) holographic model [35]. The black dashed-dotted line depicts the predictions from the non-conformal holographic model [34]. The orange area corresponds to the far-from-equilibrium time-dependent value of  $\eta/s$  in a holographic model (in a region of  $t_{avg} = 0.24 - 0.59 fm$ ) [36]. The dark red dashed-dotted line corresponds to the RTA estimations for the  $N_f = 2$  linear sigma model [40]. The dark green dashed line presents RTA estimations for the  $N_f = 3$  PNJL model [41]. For the hadronic phase  $T < T_c = 0.158$  GeV we show evaluations from transport models: URQMD (orange line with open circles) [42], SMASH (grey solid line with rhombuses) [43, 44]. The PHSD results for the hadronic phase are shown by the violet solid line with triangles while for the partonic phase given by violet solid line with circles calculated by Kubo formalism [27].

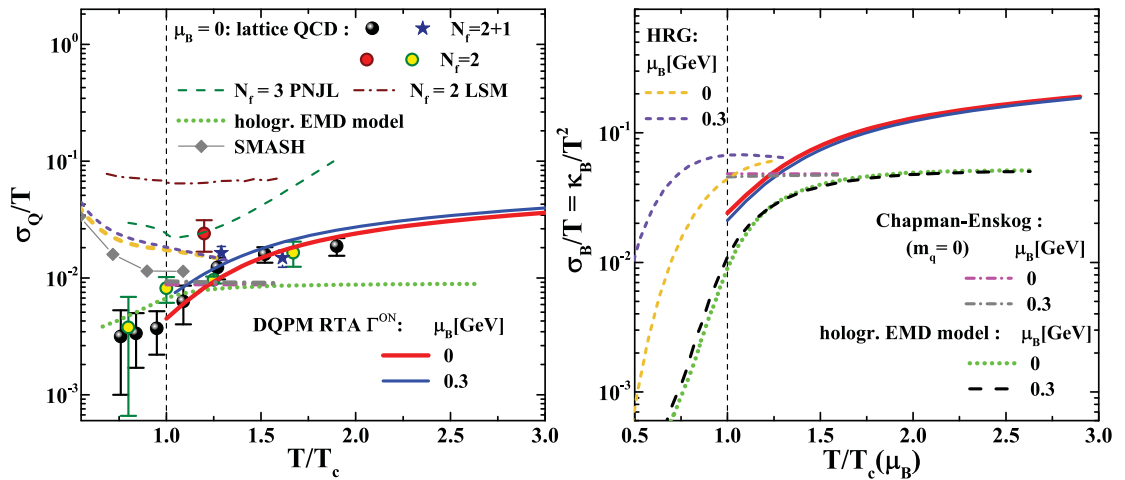


**Figure 4.** Scaled electric (Left) and baryon (Right) conductivities as a function of scaled temperature  $T/T_c$  at  $\mu_B = 0$  and  $\mu_B = 0.3$  GeV. The DQPM results obtained by the RTA approach with the interaction rate [38] are presented by the red solid lines for  $\mu_B = 0$  and by the blue solid line for  $\mu_B = 0.3$  GeV. The symbols corresponds to the IQCD results at  $\mu_B = 0$  for  $N_f = 2$ : red circle-shaped point [53], yellow circle-shaped points [54], and for  $N_f = 2 + 1$ : black spheres [55] and blue stars [56]. Violet and grey dashed lines show the estimations for the HRG model obtained within the Chapman-Enskog method [57] for  $\mu_B = 0$  and  $\mu_B = 0.3$  GeV, respectively. The light green dotted line and dashed black line correspond to the estimations from the Einstein-Maxwell-Dilaton (EMD) holographic model [35]. The grey solid line with rhombuses corresponds to the estimations from the SMASH transport model [60]. The dark red dashed-dotted line corresponds to the RTA estimations for  $N_f = 2$  linear sigma model [40]. The dark green dashed line presents RTA estimations for  $N_f = 3$  PNJL model [41].

generation and evolution of electromagnetic fields produced in HICs [49–52]. The DQPM results for the electric (left) and baryon conductivities (right) are shown in figure 4 as a function of the scaled temperature  $T/T_c$ . We find a good agreement with the IQCD calculations for  $\sigma_Q/T$  for  $N_f = 2$ : red circle-shaped point [53], yellow circle-shaped points [54], and for  $N_f = 2 + 1$ : black spheres [55] and blue stars [56]. The scaled electric and baryon conductivity have a similar temperature dependence: the ratios increase with temperature increase as  $\sim T^2$  which is mainly due to the increasing quark density with temperature. We found a good agreement in the vicinity of  $T_c$  with the estimates from the various models in the partonic sector, such as the Chapman-Enskog method, where cross-sections for massless quarks and gluons are fixed as  $\sigma_{tot} \approx 0.72/T^2$  [57], the non-conformal holographic model [35], and extended  $N_f = 3$

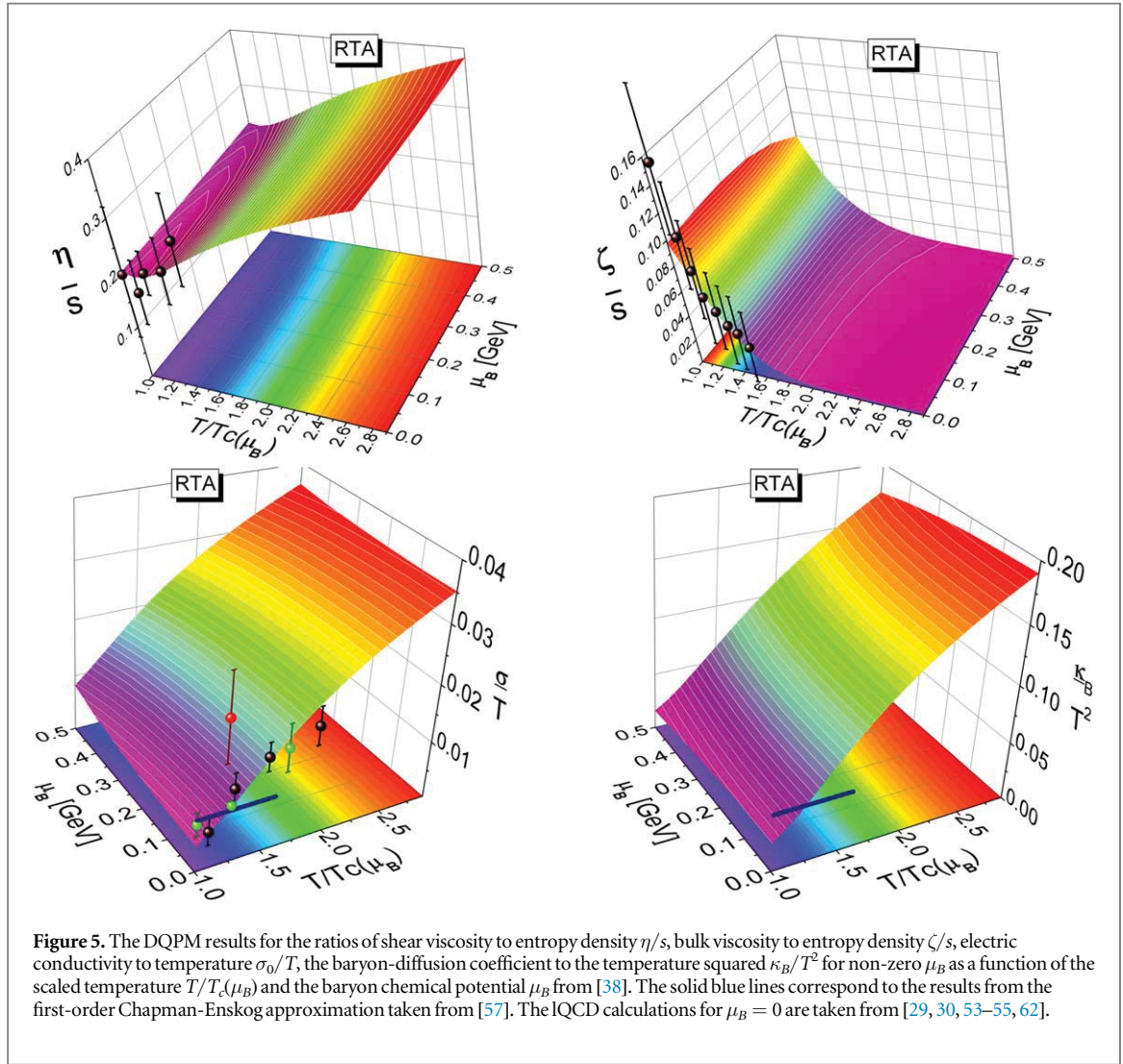


**Figure 5.** The DQPM results for the ratios of shear viscosity to entropy density  $\eta/s$ , bulk viscosity to entropy density  $\zeta/s$ , electric conductivity to temperature  $\sigma_0/T$ , the baryon-diffusion coefficient to the temperature squared  $\kappa_B/T^2$  for non-zero  $\mu_B$  as a function of the scaled temperature  $T/T_c(\mu_B)$  and the baryon chemical potential  $\mu_B$  from [38]. The solid blue lines correspond to the results from the first-order Chapman-Enskog approximation taken from [57]. The lQCD calculations for  $\mu_B = 0$  are taken from [29, 30, 53–55, 62].

PNJL model [41]. However, the temperature dependence of  $\sigma_Q/T$  differs among the various models. Furthermore, we show recent results of the scaled electric conductivity for the hadronic phase from the SMASH transport model (grey solid line with rhombuses) [43, 44], Chapman-Enskog method for the HRG model [57], and RTA estimations for  $N_f = 2$  linear sigma model [40]. There are also predictions for the electric conductivity by solving the relativistic transport equations for partons in a box with periodic boundary conditions in the presence of an external electric field as in [58, 59].

With the increase of baryon chemical potential the net baryon density increases, which influences the baryon conductivity. Figure 4 (right) shows the actual results for the baryon diffusion coefficient in the range of temperature and non-zero baryon chemical potential  $\mu_B = 0.3$  GeV as well as  $\mu_B = 0$ . We compare the DQPM results to the estimates from the non-conformal holographic model [35] and the estimates for the hadron gas within the Chapman-Enskog method [57]. In the vicinity of  $T_c$  the DQPM values for the diffusion coefficient are in agreement with the calculations within the Chapman-Enskog first-order approximation for massless quarks and gluons in [57]. Nevertheless, approaching higher temperatures the ratio  $\sigma_B^{RTA}/T$  grows with temperature in the DQPM while the Chapman-Enskog results stay nearly constant  $\sigma_B^{CE}/T \sim 0.048$ . Recently, estimates for the full diffusion coefficient matrix of the QGP have shown rather small difference between the Chapman-Enskog method in comparison to the RTA method [61], where the parton microscopic properties are described by the DQPM.

The DQPM results for non-zero baryon chemical potential, obtained within the relaxation-time approximation, are presented in figure 5 for the ratios of shear viscosity to entropy density  $\eta/s$ , bulk viscosity to entropy density  $\zeta/s$ , electric conductivity to temperature  $\sigma_0/T$ , the baryon-diffusion coefficient to the temperature squared  $\kappa_B/T^2$  for non-zero  $\mu_B$  as a function of the scaled temperature  $T/T_c(\mu_B)$  and the baryon chemical potential  $\mu_B$ . We show also the lQCD calculations for  $\mu_B = 0$  from [29, 30, 53–55, 62]. Additionally, we compare the DQPM

calculations for  $\sigma_Q/T$  and  $\sigma_B/T \equiv \kappa_B/T^2$  to the results from the first-order Chapman-Enskog approximation for a simplified pQCD medium at  $\mu_B = 0$  taken from [57] and find a reasonable agreement.

We find only a rather weak dependence of the transport coefficients on  $\mu_B$ . The shear and bulk viscosities, and electric conductivities of the QGP increase slightly with increasing  $\mu_B$  while the baryon-diffusion coefficient decreases. The latter has important consequences for the transport results for HIC observables, e.g., the baryon diffusion might enhance the difference between proton and antiproton elliptic flow  $v_2(p_T)$  and mean transverse momenta.

While at zero (or vanishing)  $\mu_B$  the transport coefficients can be extracted from the HIC data at high energies by a Bayesian analysis based on hydrodynamic model calculations (cf figure 3), at finite and large baryon chemical potential, which are probed by HICs at low and intermediate energies, this becomes conceptually difficult due to the large passing time of the colliding nuclei, which limits the applicability of hydrodynamic models. The way to overcome this difficulties has been proposed recently in [63] where  $\eta/s = 0.65 \pm 0.15$  has been extracted from the low energy Au+Au collisions at  $\sqrt{s} = 2.4$  GeV based on coarse graining analysis of the UrQMD transport simulations of the flow harmonics in comparison to the experimental data from the HADES Collaboration. According to the freeze-out line obtained by comparison of statistical model results with the experimental data [64], this corresponds to  $T \sim 70$  MeV and  $\mu_B \sim 800$  MeV where the matter contains hadronic degrees of freedom. With increasing energy of HICs the partonic degrees show up and  $\eta/s$  decreases (cf figure 5 of [63]). In [65] the  $\eta/s$  of nuclear matter produced in the central area of central Au+Au collisions at energies  $E_{lab} = 10 - 40$  A GeV (i.e.  $\mu_B \sim 600 - 400$  MeV) has been studied within the UrQMD model and a minimal value of  $\eta/s \simeq 0.3$  has been obtained. Furthermore, according to the hybrid UrQMD calculations from [66], with increasing energy range  $\sqrt{s} = 7.7 - 200$  GeV, i.e. with further lowering of  $\mu_B$  from  $\sim 400$  MeV to 25 MeV,  $\eta/s$  decrees from 0.2 to KKS boundary  $1/(4\pi)$ .

#### 4. Dynamics of the QCD at finite chemical potential

To study the evolution of the QCD medium produced in HICs one can rely on microscopic transport approaches, which provide the full time evolution of the system. Nevertheless, the evolution of the deconfined QCD phase has been successfully described within hydrodynamic simulations and hybrid methods, too. The parton-hadron-string dynamics (PHSD) approach is an off-shell transport approach based on Kadanoff-Baym equations in first-order gradient expansion which allows for simulations of both the hadronic and the partonic phases. Whereas the hadronic part is essentially equivalent to the conventional HSD approach [67], the partonic dynamics is based on the dynamical quasi-particle model (DQPM) described above. The parton-hadron phase transition (for light quarks/antiquarks) is described by the dynamical hadronization, where the fusion of quark-antiquark pairs to mesonic resonances (or three quarks (antiquarks) to baryonic states) is realized by the covariant transition rates [68, 69]. We mention that an out-of-equilibrium study on the  $\mu_B$  dependence of the QGP—created in HICs—has been performed within the PHSD transport approach, which encompass full evolution of the system including the partonic phase. The evolution of the partonic phase in the PHSD transport approach is extended by explicitly calculated the total and differential partonic scattering cross-sections based on the DQPM and evaluated at the actual temperature  $T$  and baryon chemical potential  $\mu_B$  in each individual space-time cell where partonic scattering takes place [23, 70].

We found only a small influence of a  $\mu_B$  evolution of the QGP in heavy-ion observables, since when decreasing the collision energy and thus increasing  $\mu_B$ , the QGP volume decreases rapidly and the hadronic phase becomes dominant [23, 70, 71]. Therefore even for low collision energies the influence of the QGP matter is washed out. Nevertheless, observables for strange hadrons—kaons and especially anti-strange hyperons—as well as for antiprotons show a more pronounced effect of the  $\mu_B$  dependence of QGP interactions. This gives an experimental hint for the search of finite- $\mu_B$  traces of the QGP for experiments at the future FAIR and NICA accelerators, even if it will be a very challenging experimental task.

#### 5. Conclusions and Outlook

We have presented recent results on the transport properties of the QCD at finite chemical potential. Starting with the description of the microscopic properties of the parton degrees of freedom we have discussed the transport coefficients of the partonic phase obtained within the dynamical quasi-particle model (DQPM) and compared the results at vanishing chemical potential with numerous predictions from the literature. We have found a good agreement with the available lQCD calculations for transport coefficients at  $\mu_B=0$ . Furthermore, we have shown that the presence of a non-zero chemical potential can affect the transport coefficients already in the region of moderate baryon chemical potential  $\mu_B \leq 500$  GeV, where a cross-over phase transition likely takes place.






## Acknowledgments

The authors acknowledge inspiring discussions with Jörg Aichelin, Wolfgang Cassing, Lucia Oliva and Taesoo Song. O.S. acknowledges support from the Helmholtz Graduate School for Heavy Ion research. P.M. acknowledges support by the U.S. D.O.E. under Grant No. DE-FG02-05ER41367. Furthermore, we acknowledge support by the Deutsche Forschungsgemeinschaft (DFG, German Research Foundation): grant CRC-TR 211 Strong-interaction matter under extreme conditions' - Project number 315 477 589—TRR 211; by the European Unions Horizon 2020 research and innovation program under grant agreement No 824 093 (STRONG-2020) and by the COST Action THOR, CA15213. The computational resources have been provided by the LOEWE-Center for Scientific Computing and the 'Green Cube' at GSI, Darmstadt.

## Data availability statement

No new data were created or analysed in this study.

## ORCID iDs

Olga Soloveva  <https://orcid.org/0000-0002-8833-4384>  
 Pierre Moreau  <https://orcid.org/0000-0003-1812-1751>  
 Elena Bratkovskaya  <https://orcid.org/0000-0002-8228-3811>

## References

- [1] Arsene I *et al* (BRAHMS) 2005 *Nucl. Phys. A* **757** 1–27
- [2] Adams J *et al* (STAR) 2005 *Nucl. Phys. A* **757** 102–83
- [3] Shuryak E V 1978 *Phys. Lett. B* **78** 150
- [4] Gyulassy M and McLerran L 2005 *Nucl. Phys. A* **750** 30–63
- [5] Odyniec G and (STAR) 2019 Beam energy scan program at RHIC (BES I and BES II) – probing QCD phase diagram with heavy-ion collisions *PoS* **341** 151
- [6] Senger P 2020 *JPS Conf. Proc.* **32** 010092
- [7] Sissakian A, Sorin A and (NICA) 2009 *J. Phys. G* **36** 064069
- [8] Peshier A and Cassing W 2005 *Phys. Rev. Lett.* **94** 172301
- [9] Cassing W 2007 *Nucl. Phys. A* **795** 70–97
- [10] Cassing W 2007 *Nucl. Phys. A* **791** 365–81
- [11] Borsanyi S, Endrodi G, Fodor Z, Katz S, Krieg S, Ratti C and Szabo K 2012 *J. High Energy Phys.* **JHEP08(2012)053**
- [12] Borsanyi S, Fodor Z, Hoelbling C, Katz S D, Krieg S and Szabo K K 2014 *Phys. Lett. B* **730** 99–104
- [13] Cassing W 2009 *Eur. Phys. J. ST* **168** 3–87
- [14] Berrehrah H, Bratkovskaya E, Steinert T and Cassing W 2016 *Int. J. Mod. Phys. E* **25** 1642003
- [15] Cea P, Cosmai L and Papa A 2016 *Phys. Rev. D* **93** 014507
- [16] Guenther J N 2020 arXiv: [2010.15503](https://arxiv.org/abs/2010.15503)
- [17] Borsanyi S, Fodor Z, Guenther J N, Kara R, Katz S D, Parotto P, Pasztor A, Ratti C and Szabo K K 2020 *Phys. Rev. Lett.* **125** 052001
- [18] Bazavov A *et al* (HotQCD) 2019 *Phys. Lett. B* **795** 15–21
- [19] Bellac M L 2011 *Thermal Field Theory Cambridge Monographs on Mathematical Physics* (Cambridge: Cambridge University Press)
- [20] Linnyk O, Bratkovskaya E and Cassing W 2016 *Prog. Part. Nucl. Phys.* **87** 50–115
- [21] Vanderheyden B and Baym G 1998 *J. Stat. Phys.* **93** 843
- [22] Blaizot J P, Iancu E and Rebhan A 2001 *Phys. Rev. D* **63** 065003
- [23] Moreau P, Soloveva O, Oliva L, Song T, Cassing W and Bratkovskaya E 2019 *Phys. Rev. C* **100** 014911
- [24] Ryu S, Paquet J F, Shen C, Denicol G S, Schenke B, Jeon S and Gale C 2015 *Phys. Rev. Lett.* **115** 132301
- [25] Kubo R 1957 *J. Phys. Soc. Jap.* **12** 570–86
- [26] Aarts G and Martinez Resco J M 2002 *J. High Energy Phys.* **JHEP04(2002)053**
- [27] Ozvenchuk V, Linnyk O, Gorenstein M I, Bratkovskaya E L and Cassing W 2013 *Phys. Rev. C* **87** 064903
- [28] Chakraborty P and Kapusta J 2011 *Phys. Rev. C* **83** 014906
- [29] Astrakhantsev N, Braguta V and Kotov A 2017 *J. High Energy Phys.* **JHEP04(2017)101**
- [30] Astrakhantsev N, Braguta V and Kotov A 2018 *Phys. Rev. D* **98** 054515
- [31] Nakamura A and Sakai S 2005 *Phys. Rev. Lett.* **94** 072305
- [32] Meyer H B 2008 *Phys. Rev. Lett.* **100** 162001
- [33] Meyer H B 2007 *Phys. Rev. D* **76** 101701
- [34] Attems M, Casalderrey-Solana J, Mateos D, Papadimitriou I, Santos-Oliván D, Sopena C F, Triana M and Zilhão M 2016 *J. High Energy Phys.* **JHEP10(2016)155**
- [35] Rougemont R, Critelli R, Noronha-Hostler J, Noronha J and Ratti C 2017 *Phys. Rev. D* **96** 014032
- [36] Wondrak M F, Kaminski M and Bleicher M 2020 *Phys. Lett. B* **811** 135973
- [37] Bernhard J E, Moreland J S and Bass S A 2019 *Nature Phys.* **15** 1113–7
- [38] Soloveva O, Moreau P and Bratkovskaya E 2020 *Phys. Rev. C* **101** 045203
- [39] Kovtun P, Son D T and Starinets A O 2005 *Phys. Rev. Lett.* **94** 111601
- [40] Heffernan M, Jeon S and Gale C 2020 *Phys. Rev. C* **102** 034906

- [41] Soloveva O, Fuseau D, Aichelín J and Bratkovskaya E 2020 arXiv:[2011.03505](#)
- [42] Demir N and Bass S A 2009 *Phys. Rev. Lett.* **102** 172302
- [43] Rose J B, Torres-Rincon J M, Schäfer A, Oliinychenko D R and Petersen H 2018 *Phys. Rev. C* **97** 055204
- [44] Rose J B, Torres-Rincon J M and Elfner H 2020 *J. Phys. G* **48** 015005
- [45] Borsanyi S, Endrodi G, Fodor Z, Jakovac A, Katz S D, Krieg S, Ratti C and Szabo K K 2010 *J. High Energy Phys.* [JHEP11\(2010\)077](#)
- [46] Turbide S, Rapp R and Gale C 2004 *Phys. Rev. C* **69** 014903
- [47] Akamatsu Y, Hamagaki H, Hatsuda T and Hirano T 2011 *J. Phys. G* **38** 124184
- [48] Yin Y 2014 *Phys. Rev. C* **90** 044903
- [49] Tuchin K 2013 *Phys. Rev. C* **88** 024911
- [50] Inghirami G, Mace M, Hirono Y, Del Zanna L, Kharzeev D E and Bleicher M 2019
- [51] Denicol G S, Molnár E, Niemi H and Rischke D H 2019 *Phys. Rev. D* **99** 056017
- [52] Oliva L 2020 *Eur. Phys. J. A* **56** 255
- [53] Brandt B B, Francis A, Meyer H B and Wittig H 2013 *J. High Energy Phys.* [JHEP03\(2013\)100](#)
- [54] Brandt B B, Francis A, Jäger B and Meyer H B 2016 *Phys. Rev. D* **93** 054510
- [55] Aarts G, Allton C, Amato A, Giudice P, Hands S and Skullerud J I 2015 *J. High Energy Phys.* [JHEP02\(2015\)186](#)
- [56] Astrakhantsev N, Braguta V V, D'Elia M, Kotov A Y, Nikolaev A A and Sanfilippo F 2020 *Phys. Rev. D* **102** 054516
- [57] Greif M, Fotakis J A, Denicol G S and Greiner C 2018 *Phys. Rev. Lett.* **120** 242301
- [58] Cassing W, Linnyk O, Steinert T and Ozvenchuk V 2013 *Phys. Rev. Lett.* **110** 182301
- [59] Puglisi A, Plumari S and Greco V 2014 *Phys. Rev. D* **90** 114009
- [60] Rose J B, Greif M, Hammelmann J, Fotakis J A, Denicol G S, Elfner H and Greiner C 2020 *Phys. Rev. D* **101** 114028
- [61] Fotakis J A, Soloveva O, Greiner C, Kaczmarek O and Bratkovskaya E 2021 *Phys. Rev. D* **104** 034014
- [62] Amato A, Aarts G, Allton C, Giudice P, Hands S and Skullerud J I 2013 *Phys. Rev. Lett.* **111** 172001
- [63] Reichert T, Inghirami G and Bleicher M 2021 *Phys. Lett. B* **817** 136285
- [64] Cleymans J, Oeschler H, Redlich K and Wheaton S 2006 *Phys. Rev. C* **73** 034905
- [65] Teslyk M, Bravina L, Panova O, Vitiuk O and Zabrodin E 2020 *Phys. Rev. C* **101** 014904
- [66] Karpenko I A, Huovinen P, Petersen H and Bleicher M 2015 *Phys. Rev. C* **91** 064901
- [67] Cassing W and Bratkovskaya E 1999 *Phys. Rept.* **308** 65–233
- [68] Cassing W and Bratkovskaya E 2009 *Nucl. Phys. A* **831** 215–42
- [69] Bratkovskaya E, Cassing W, Konchakovski V and Linnyk O 2011 *Nucl. Phys. A* **856** 162–82
- [70] Soloveva O, Moreau P, Oliva L, Voronyuk V, Kireyeu V, Song T and Bratkovskaya E 2020 *Particles* **3** 178–92
- [71] Moreau P, Soloveva O, Grishmanovskii I, Voronyuk V, Oliva L, Song T, Kireyeu V, Coci G and Bratkovskaya E 2021 Properties of the QGP created in heavy-ion collisions *Astron.Nachr.* **342** 715–26